Nanosecond laser annealing: Impact on superconducting silicon on insulator monocrystalline epilayers

Y. Baron [ID] ; J. L. Lábár [ID] ; S. Lequien; B. Pécz [ID] ; R. Daubriac [ID] ; S. Kerdilès [ID] ; P. Acosta Alba [ID] ;
C. Marcenat [ID] ; D. Débarre [ID] ; F. Lefloch [✉] [ID] ; F. Chiodi [✉] [ID]

Check for updates

View Online   Export Citation

Articles You May Be Interested In

High-mobility diamond field effect transistor with a monocrystalline h-BN gate dielectric

APL Mater. (November 2018)

Comparative analysis on photovoltaic thermal (PVT) system using monocrystalline silicon and polycrystalline silicon modules

AIP Conf. Proc. (August 2024)

Investigation of monocrystalline p-type PERC cells featuring the laser enhanced contact optimization process and new LECO paste

AIP Conference Proceedings (June 2021)

Nanosecond laser annealing: Impact on superconducting silicon on insulator monocrystalline epilayers

View Online   Export Citation   CrossMark

Y. Baron,[1] [ID] J. L. Lábár,[2] [ID] S. Lequien,[3] B. Pécz,[2] [ID] R. Daubriac,[4] [ID] S. Kerdilès,[4] [ID] P. Acosta Alba,[4] [ID]
C. Marcenat,[5] [ID] D. Débarre,[1] [ID] F. Lefloch,[5,a] [ID] and F. Chiodi[1,a] [ID]

AFFILIATIONS

[1] University Paris-Saclay, CNRS, Centre de Nanosciences et de Nanotechnologies, 91120 Palaiseau, France
[2] Thin Film Physics Laboratory, Institute of Technical Physics and Materials Science, Centre of Energy Research, Konkoly Thege M. u. 29-33, H-1121 Budapest, Hungary
[3] University Grenoble Alpes, CEA, IRIG-MEM, 38000 Grenoble, France
[4] University Grenoble Alpes, CEA, LETI, Minatec Campus, 38000 Grenoble, France
[5] University Grenoble Alpes, CEA, Grenoble INP, IRIG-PHELIQS, 38000 Grenoble, France

[a] Authors to whom correspondence should be addressed: francois.lefloch@cea.fr and francesca.chiodi@c2n.upsaclay.fr

ABSTRACT

We present superconducting monocrystalline silicon-on-insulator thin 33 nm epilayers. They are obtained by nanosecond laser annealing under ultra-high vacuum on 300 mm wafers heavily pre-implanted with boron (2.5×10^{16} at./cm^2, 3 keV). Superconductivity is discussed in relation to the structural, electrical, and material properties, a step toward the integration of ultra-doped superconducting Si at large scale. In particular, we highlight the effect of the nanosecond laser annealing energy and the impact of multiple laser anneals. Increasing the energy leads to a linear increase in the layer thickness and to the increase in the superconducting critical temperature T_c from zero (< 35 mK) to 0.5 K. This value is comparable with superconducting Si layers realized by gas immersion laser doping, where dopants are incorporated without introducing the deep defects associated with implantation. Superconductivity only appears when the annealed depth exceeds the initial amorphous layer induced by the boron implantation. Multiple subsequent anneals result in a more homogeneous doping with reduced amount of structural defects and increased conductivity. The quantitative analysis of T_c concludes on a superconducting–non-superconducting bilayer with an extremely low resistance interface. This highlights the possibility to efficiently couple superconducting Si to Si channels.

INTRODUCTION

In the context of solid-state based quantum engineering, materials science remains a very active field of research. Recent reviews[1–4] point out the importance of controlling both the quality of materials, to prevent/reduce quantum decoherence,[5,6] and the reproducibility, in the prospect of scaling-up quantum technology toward a very large number of qubits. In this quest of large scale integration, silicon and germanium can be seen as the short-term most promising materials.[7,8] However, they are currently restricted to spin qubits, where the rather low yield in the quantum properties has limited

the demonstration of coupled qubits to a very small number,[9] in contrast to superconducting transmons qubits, where operations with few tens of qubits have been recently demonstrated.[10,11] The possibility to fabricate superconducting qubits with silicon would offer both the advantages of a mature technology and superconductivity. In principle, this could be achieved with superconducting silicon, obtained by combining heavily boron doping and nanosecond laser annealing.[12–16] However, implementation of superconducting Si:B into quantum circuits is still at its early stage[17–20] and a better understanding of the superconducting properties is still required, especially within the constraints of compatible large

02 December 2024 20:30:12

scale integration tools. In the present study, we investigate the superconducting properties of boron-doped superconducting silicon epilayers obtained on 33 nm thick SOI (silicon on insulator) 300 mm wafers after pre-implantation of boron dopants, followed by nanosecond laser annealing. Our results demonstrate a continuous increase in the superconducting critical temperature T_c as a function of melted depth tuned by the laser energy and the weak impact of implantation-induced defects. A maximum T_c of about 0.5 K is reached when the entire 33 nm thick silicon layer is melted, producing a crystalline structure, while no superconductivity is observed when the annealing only affects the surface amorphous layer induced by the strong dopant implantation. We emphasize the role of identical multiple laser shots by comparing a series of sample having sustained 1 or 5 laser shot annealings, highlighting the decrease in defects and better homogeneity with an increased number of shots. The T_c variation is well-described by a two-layer model (one being superconducting and the other not) connected through a high transparency interface. This indicates the possibility to optimally couple the superconducting layer to silicon channels through low resistance interfaces.

Nanosecond annealing of B implanted SOI

The first step of the fabrication of superconducting SOI layers is the implantation of a very high boron dose (2.5×10^{16} cm^{-2}) at 3 keV, at tilt 7° and twist 22°, on a non-intentionally doped 300 mm wafer. The initial SOI wafer has a silicon layer 33 ±1 nm thick on top of a SiO$_2$ buried oxide layer (BOX) of 20 nm, as in Ref. 15. After the implantation, the SOI layer is composed of an amorphous layer (a-Si) of 15 ± 1 nm on top of the remaining silicon crystalline layer (c-Si) (see Fig. 4a in Ref. 15). CTRIM simulations show that the dopant's concentration in the underneath c-Si layer remains significant (above 1 at. % percent).[21]

The nanosecond laser annealing process is performed with an excimer XeCl laser of pulse duration 25 ns under UHV (ultra-high vacuum) conditions ($P = 10^{-9}$ mbar) with energy density at the sample level $E_L = 300$–600 mJ/cm^2 ($E_L = 600$ mJ/cm^2 corresponding to the bulk Si melting threshold). The effect of the laser pulse is to melt the top of the implanted silicon layer, over a 2×2 mm^2 surface with laser energy homogeneity of 1.2%, during ≈ 15 to 25 ns. This induces an extremely fast re-crystallization, activating the dopants up to a saturation concentration of $n_{sat} = 3 \times 10^{21}$ cm^{-3} (6 at. %), an order of magnitude above the solubility limit $n_{sol} \sim 4 \times 10^{20}$ cm^{-3}.[22] The thickness of the melted layer linearly depends on the laser energy at the sample level. The time-resolved reflectometry (TRR) of a red ($\lambda = 675$ nm) laser is recorded *in situ* during the nanosecond laser annealing to follow the melting–solidification process, and its value is compared to bare, undoped, Si reflectivity $\mathcal{R}_{Si}$ [Fig. 1(a)].

For the present study, two series of laser spots have been generated. For the first series, each spot has been patterned after the laser annealing to define Hall cross structures with Ti/Au contact pads allowing precise measurement of the square and Hall resistances. The second series of spots remained untreated, for x-ray diffraction (XRD) analysis. For both series, we have measured the resistance as a function of temperature down to ≈35 mK to extract the superconducting transition temperature T_c as a function of the laser energy E_L. We emphasize the precise control over E_L, and the impact of the sharp, flat, few-nanometer-thick interface at the bottom of the
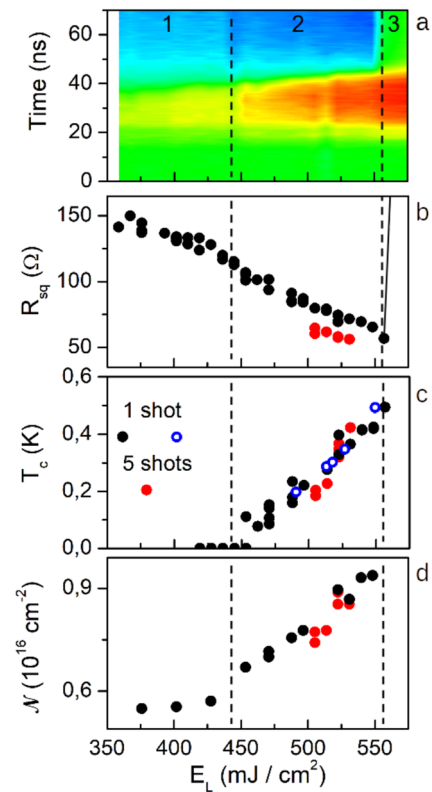
FIG. 1. Combined plot of time-resolved reflectometry (TRR) (a), room temperature square resistance R_{sq} (b), superconducting critical temperature T_c (c), and measured active carriers surface density ($\mathcal{N}$) (d) as a function of the laser energy density E_L. The dotted line at $E_L = 445$ mJ/cm^2 indicates the crossover from a polycrystalline boron doped layer (regime 1) to a crystalline epilayer (regime 2). The dotted line at $E_L = 560$ mJ/cm^2, where R_{sq} diverges, corresponds to the full melt of the initial silicon on the insulator layer as the annealing touches the amorphous SiO$_2$ BOX (regime 3). The *TRR* color plot scale corresponds to the measured TRR amplitude from 0.75 $\mathcal{R}_{Si}$ (dark blue) and 2.26 $\mathcal{R}_{Si}$ (red), and is a signature of the layer structure: amorphous (green), polycrystalline (light blue), monocrystalline (dark blue), and liquid (red). The laser pulse starts at t = 10 ns.

annealed layer, which allows, within the 33 nm SOI, fine-tuning of the depth using E_L to a precision of 1–2 nm. The overall results for the time resolved reflectivity *TRR*, the square resistance R_{sq}, the superconducting transition temperature T_c, and the active dopants dose $\mathcal{N}$ measured by the Hall effect are shown in Fig. 1 as a function of the laser energy density E_L.

We can identify three regimes. The first regime (regime 1) is for $E_L < 445$ mJ/cm^2, where no superconductivity is observed. The second regime (regime 2) applies for 445 mJ/cm$^2 < E_L < 560$ mJ/cm^2 with an almost linear increase in T_c up to a maximum value of 0.5 K. For $E_L > 560$ mJ/cm^2 (regime 3), the entire silicon layer is full-melted, the resistance diverges, and no superconductivity is observed.

We observe important differences to the results of Ref. 15, where the annealing was performed on the *same* implanted layers under N$_2$ with a similar XeCl excimer laser but of longer laser pulse duration (160 ns instead of 25 ns). In the present work, we achieve

T_c tunable up to 0.5 K, with a superconducting phase only observed in monocrystalline layers below the full melt threshold, as opposed to the constant $T_c \sim 0.18$ K obtained only in a poly-crystalline layer above the full melt in Ref. 15. Our results are instead more similar to what was observed for the longer annealing of 160 ns but with an increased ion implantation energy, from 3 to 4 keV, for which monocrystalline films were shown to be superconducting at $T_c = 0.39$ K .[16] Thus, the recrystallization dynamics seems to be strongly dependent on the laser pulse duration, even for relatively small changes (25–160 ns).

Explosive crystallization, monocrystalline SiB, and full-melt

Figure 1 shows the drastically different behavior observed in the three regimes: the explosive crystallization regime (1), the monocrystalline regime (2), and the full melt regime (3). In regime 1, an explosive re-crystallization of the doped amorphous Si (a-Si) takes place, followed by the partial melting of the resulting poly-crystalline Si (poly-Si). In this dynamic scenario,[23] even for weak laser energy, a thin layer of the initial top a-Si melts. The transition from solid to liquid occurs during the first nanoseconds of the laser pulse. This thin layer re-solidifies almost instantly into poly-Si and the latent heat released during this liquid to solid transformation is sufficient to progressively melt the a-Si underneath. The process stops when the entire initial a-Si is totally transformed into poly-Si, as the energy is not sufficient to melt crystalline Si. During the remaining time of the laser pulse, as the laser energy increases above the poly-Si melting threshold, the just-formed poly-Si is melted over a depth that depends linearly with the laser energy density. In regime 1, the entire a-Si is, therefore, transformed into poly-Si with a final thickness independent of the laser energy, with part of the poly-Si having been remelted. This results in a variation of reflectivity from the initial amorphous state at $\mathcal{R}_a = 1.52 \, \mathcal{R}_{Si}$ to the polycrystalline state $\mathcal{R}_{poly} = 1.05 \, \mathcal{R}_{Si}$ [Fig. 1(a)]. The square resistance varies only slightly with the laser energy density and the small decrease observed is due to the re-arrangement of poly-crystals and a slightly better activation as a consequence of the poly-Si melting [Fig. 1(b)]. Correspondingly, the active dose ($\mathcal{N}$) measured by the Hall effect is nearly constant and independent of E_L [Fig. 1(c)]. From the laser energy density that characterizes regime 1, we estimate the thickness of the poly-Si layer to ≈ 18.5 nm, close to the initial a-Si layer thickness.[15]

In regime 2, the laser energy density is strong enough to melt the entire poly-Si created by explosive recrystallization from the a-Si layer, plus a thin part of the crystalline c-Si layer underneath. In that situation, the poly-Si is entirely melted and transformed into a boron doped monocrystalline silicon Si:B epilayer from the remaining weakly doped c-Si seed. This can be observed in the TRR map as the reflectivity first peaks as a result of the explosive crystallization [Fig. 1(a), yellow line at $t \sim 20$ ns, $\mathcal{R}_{ec} = 1.82 \, \mathcal{R}_{Si}$] and then increases to the melted phase (red, $\mathcal{R}_{melt} = 2.2 \, \mathcal{R}_{Si}$) to finally cool down to a monocrystal (blue, $\mathcal{R}_{mono} = 0.95 \, \mathcal{R}_{Si}$). The final thickness of the Si:B layer on top of the c-Si depends linearly on the laser energy density (Fig. 3, supplementary material.). The active dose ($\mathcal{N}$) increases with E_L [Fig. 1(d)] due to the incorporation and activation of an increasing amount of implanted dopants in the Si:B layer. It should be noted that the measured $\mathcal{N}$ is always lower

than the initial implanted dose (at most 38%), as the Hall effect only measures the active dose. From the TRR maps, the identification of the full melt ($d_{melt} = d_{SOI}$) and the corresponding dose ($\mathcal{N}_{FM}$), it is possible to extract the active concentration of the thickest monocrystalline layer, $\mathcal{N}_{FM}/d_{SOI} = 2.9 \times 10^{21} \text{cm}^{-3}$. The active concentration for the thinnest monocrystalline layer is likewise calculated to be 3.1×10^{21} cm^{-3}. This suggests that the layers present a nearly constant active concentration $n_{sat} \approx 3 \times 10^{21}$ cm^{-3}, equal within 7% for all the layers, as also confirmed by the nearly constant position of the Si:B XRD peak (Fig. 1, supplementary material.). Similarly, a saturation of the active concentration $n_{sat} = 2.8$–3.1×10^{21} cm^{-3} was observed in bulk Si:B layers in the same 23–47 nm thickness range.[22] Those layers, realized by gas immersion laser doping (GILD), employed nanosecond laser annealing with exactly the same laser, but with a BCl$_3$ gas precursor. The active concentration limit could thus be associated not to the dopant incorporation method, but to the maximum recrystallization speed (~ 4 m/s)[24] induced by the 25 ns pulse duration.

As the Si:B layer becomes thicker, the square resistance decreases smoothly with E_L [Fig. 1(b)]. One can notice that the square resistance after one laser shot is larger than that after five shots. This can be understood as, on one side, the crystalline quality slightly improves upon repeated annealing, and on the other, the homogeneity of the boron is increased as the dopants initially present in the top of the layer have more time to diffuse within the whole melted layer. In regime 2, the superconducting temperature transition grows from $T_C < 35$ mK (35 mK is the minimum transition temperature we could measure in our cryostat) to 0.5 K just before reaching the full-melt regime 3 [Fig. 1(c)]. Contrary to the R_{sq} behavior, the T_c difference between 1 and 5 shot(s) is less marked.

Finally, regime 3 is reached when the laser energy is large enough that the entire silicon layer melts (full melt threshold) and an amorphous Si:B layer builds up on the underneath amorphous SiO$_2$, recovering the initial amorphous reflectivity $R_a/R_{in} = 1.06$ [Fig. 1(a)]. As a result, R_{sq} diverges up to 100 kΩ and superconductivity is suppressed [Figs. 1(b) and 1(c)]. We highlight that superconductivity is thus exclusively observed in monocrystalline Si:B layers, with a maximum T_c for laser energies just before the full melt.

Superconductivity and number of laser pulses

In order to better understand the impact of multiple laser shots on both the superconducting and the normal state, we complemented our transport measurements and x-ray diffraction data with transmission electronic microscopy (TEM). We show in Fig. 2 the comparison between two samples in regime 2 having the same active dose, realized with the same laser energy $E_L = 522$ mJ/cm^2 where nearly all the Si has been melted ($d_{melt} = 29$ nm), with 1 or 5 laser shots. The TEM images show from left to right the Si substrate, the SiO$_2$ BOX, and the B-implanted Si layer, where the laser annealing took place, and a capping layer introduced to protect the layer during TEM sample preparation. The interface between melted and unmelted SiB is difficult to discern in these particular samples as it is only ~ 2 nm away from the BOX and as the doping increases gradually over a few nanometers from the bottom of the SiB layer.[25]

Performing a few laser shots, as opposed to a single one, impacts the sublayer structure, apparent within the laser annealed
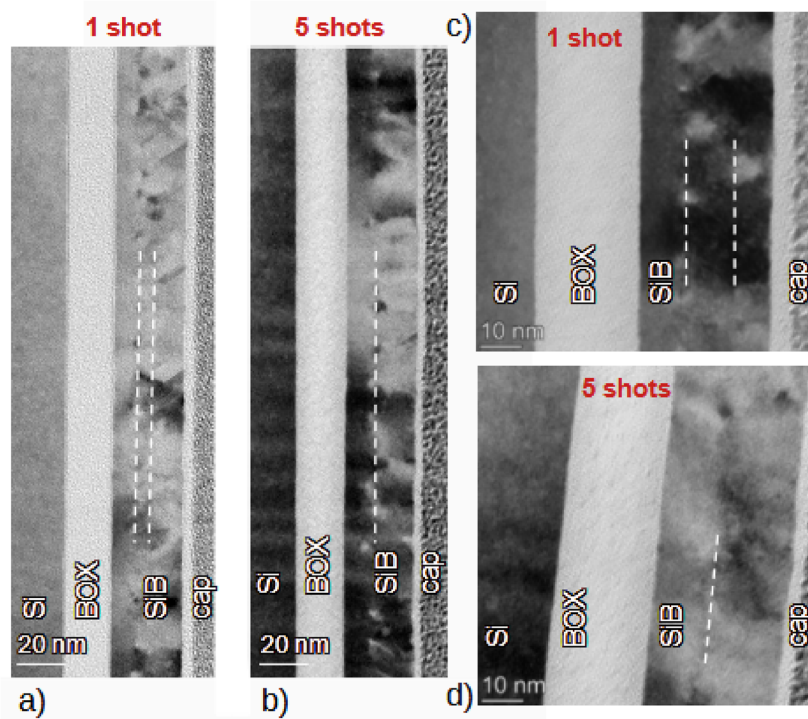
FIG. 2. TEM images of two samples realized with 1 (a) and (c) or 5 (b) and (d) laser pulses at E_L = 522 mJ/cm^2 (d_{melt} = 29 nm). Visible from left to right are the Si substrate, the SiO$_2$ BOX, and the B-implanted Si layer, where the laser annealing took place, and a capping layer for TEM. The dotted lines mark the alignment of the dislocations and stacking faults, as a result of strain relaxation.

SiB, and results in a decreased disorder. A larger amount of structural defects is indeed present after a single laser annealing, with dislocations and stacking faults originating from two interfaces located approximately 10 nm and 17–21 nm above the BOX. These interfaces are formed between a fully strained sublayer on the bottom, a partially relaxed middle sublayer with a gradually increasing deformation, and a top sublayer with a constant deformation (Fig. 4, supplementary material.). In comparison, the sample realized with 5 laser shots is more homogeneous, with fewer defects starting 13 nm above the BOX, and lower deformation (Fig. 4, supplementary material.). These differences can be attributed to an incomplete B diffusion, from the higher implanted concentration at the top toward the bottom, during the short (~20 ns) melting time of a single laser shot. In contrast, five laser shots allow for a longer diffusion time (about 100 ns), leading to a more homogeneous dopant concentration.

These observations are in agreement with the electrical measurements: 1 shot samples systematically show a higher resistance (Fig. 1) and a residual resistance ratio RRR = R_{300K}/R_{4K} closer to unity, indicating that the resistance at low temperature can be mostly attributed to impurities and crystallographic defects as opposed to thermal scattering. As an example, the two samples shown in Fig. 2 have RRR = 1.1 and RRR = 1.28 for one shot and five shots, respectively. Similarly, XRD data show a better crystalline quality for the five shot samples, highlighted by higher amplitude of the diffraction peak (Figs. 1 and 2, supplementary material).

In addition, we have plotted (Fig. 3) the square conductance G_{sq} ($1/R_{sq}$) as a function of the dose $\mathcal{N}$ for two series of one shot and five shots samples. The two series show a linear $G_{sq}(\mathcal{N})$ dependence, which is consistent with the simple Drude formula

$G_{sq} = e\mu\mathcal{N}$, where e is the electronic charge and μ the carriers mobility. The mobility obtained by the linear fit is μ = 12.7 cm^2 V^{-1} s^{-1}, a value in agreement with past measurements for such doping levels.[26] However, this linear fit does not extrapolate to the x axis
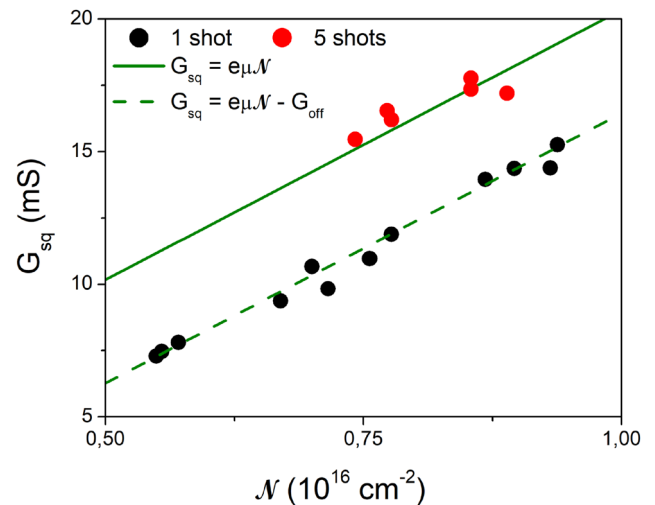
FIG. 3. Square conductance (inverse of R_{sq}) as a function of the active dopants density $\mathcal{N}$ measured with the Hall effect for both one and five shots series. The dotted line is a linear fit on the one shot series from which we can extract a mobility of 12.7 cm^2 V^{-1} s^{-1}. The solid line has the exact same slope (corresponding to the same mobility) but passes though the origin of the graph at (0,0). The negative offset corresponds to additional scattering mechanisms in the one shot series and is not present for the five shots series.

origin for the one shot series (dotted line), whereas it does for the five shots series (solid line). The difference can be explained by the existence of a bilayer (or multilayer) structure for the one shot series, with one layer more disordered than the other. Then, we have $G_{sq}^{1shot} = e\mu\mathcal{N}_1 + e\mu'\mathcal{N}_2 < G_{sq}^{5shots} = e\mu\mathcal{N}$ with $\mu' < \mu$. Plotting G_{sq} vs $\mathcal{N} = \mathcal{N}_1 + \mathcal{N}_2$, gives $G_{sq}^{1shot} = e\mu(\mathcal{N}_1 + \mathcal{N}_2) - e(\mu - \mu')\mathcal{N}_2$, with a negative offset such as the one shown in Fig. 3. From the offset amplitude, it is also possible to roughly estimate the thickness of the poorly conducting layer: taking the saturation active concentration in the whole annealed layer ($n \sim 3 \times 10^{21}$ cm^{-3}) and assuming $\mu \gg \mu' \sim 0$, from $\Delta G_{sq} = 3.9$ mS $= e\mu\mathcal{N}_2 = e\mu n_2 d_2$, we deduce $d_2 \sim 6.5$ nm. For such rough estimation, this layer thickness is comparable, although smaller, to the 7–11 nm thickness of the central sublayer in 1 shot sample (Fig. 2), where a high density of stacking faults and dislocations is observed. This suggests that the very disordered layer has a small (non-zero) μ', while the 5 shots samples have homogeneous mobility.

Superconductivity and laser energy

We now focus on the strong energy dependence of the superconducting critical temperature. As the laser energy directly affects the melted thickness, we plot T_c vs d_{melt} in Fig. 4 (see the supplementary material for details on the determination of d_{melt}). For both one and five laser shots, T_c increases steeply with the thickness of up to 0.5 K. To understand the critical temperature dependence with thickness, we recall that the melted ultra-doped layer is on top of the remaining unmelted Si above the BOX, where an implanted concentration above $\sim$1 at. % is expected. In bilayer structures made of one superconducting (S) layer in contact with a second normal (N) layer, a strong suppression of T_c can take place, if the interface between the two layers is transparent. This is only observed when the thickness of the S layer is smaller or of the order of the superconducting coherence length, as is our case with $d_{melt} < 33$ nm $< \xi \approx 50$ nm.[22] This effect, known as the inverse proximity effect, was already observed on superconducting Si layers realized in bulk Si samples[27] and is well-described with the Usadel model,[28–30]

$$T_c = T_{c0}\left[\frac{T_{c0}}{1.14\Theta_D}\sqrt{1 + \left(\frac{k_B\Theta_D}{\tau}\right)^2}\right]^{\frac{bd_N}{d_S}}, \qquad (1a)$$

$$\tau = \frac{\hbar}{2\pi}\frac{v_{F,S}}{\rho_{int}}\frac{bd_N + d_S}{bd_Nd_S}, \qquad (1b)$$

$$b = \frac{v_{F,S}}{v_{F,N}} = \left(\frac{n_N}{n_S}\right)^{1/3}, \qquad (1c)$$

where T_{c0} is the superconducting critical temperature of the single S layer, Θ_D is the phonon energy scale in temperature units, d_N (d_S) is the thickness, $v_{F,N}$ ($v_{F,S}$) is the Fermi velocity, and n_N (n_S) is the active dopant concentration in the normal (superconducting) layer.[14] ρ_{int} is the dimensionless interface resistance per channel, related to the total interface resistance per unit area A by $R_{int}A = h/2e^2 (\lambda_{F,S}/2)^2 \rho_{int}$.

The first noteworthy result is that it is possible to describe the $T_c(d_{melt})$ dependence with zero interface resistance ($\rho_{int} = 0$), for
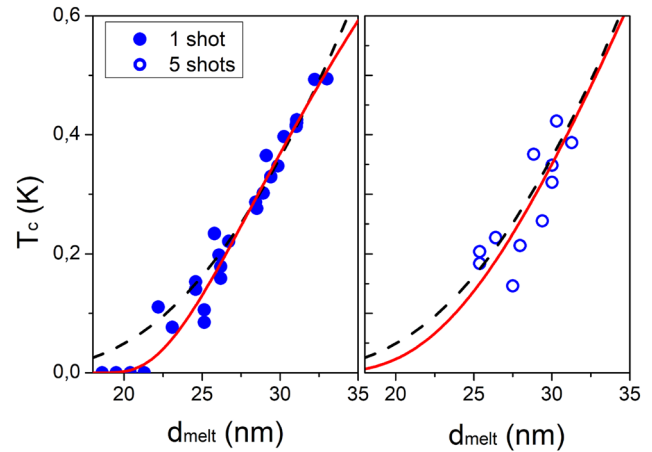

FIG. 4. T_c vs laser-melted thickness d_{melt} for both one and five laser shots. The black dotted line, plotted in both the one and five laser shots panel, shows the two-parameter fit, in the hypothesis of $d_S = d_{melt}$, with $T_{c,0} = 0.52$ K and $b = 0.5$. The red continuous line shows the three-parameter fit with the hypothesis that the superconducting layer corresponds to the relaxed portion of the melted layer, with $T_{c,0} = 1.04$ K, $b = 0.108$, and $d_S = d_{melt} - 16.6$ nm for one shot and $T_{c,0} = 1.04$ K, $b = 0.29$ and $d_S = d_{melt} - 9$ nm for five shots.

both one and five laser shots, highlighting a very good transparency. Even more, all the fits imposing a small but finite interface are, although in reasonable agreement, less satisfactory than the one at zero interface. Thus, Eq. (1) simplifies to

$$T_c = T_{c0}\left[\frac{T_{c0}}{1.14\Theta_D}\right]^{\frac{bd_N}{d_S}}. \qquad (2)$$

To reduce the number of free fitting parameters, we fix Θ_D, of weak influence on the fit, to its simulated value $\Theta_D = 650$ K.[31] The simplest thicknesses choice consists in associating the superconducting layer to the melted layer. Thus, the superconducting and normal layer thicknesses are $d_S = d_{melt}$ and $d_N = d_{SOI} - d_{melt}$. The remaining fitting parameters are $T_{c,0}$ and the ratio of the Fermi velocities $b = v_{F,S}/v_{F,N}$. The best fit of $T_c(d_{melt})$ for the whole datasets containing one and five laser shots results is given by $T_{c,0} = 0.52$ K and $b = 0.5$ (Fig. 4). The fitted $T_{c,0}$ corresponds well to the critical temperature $T_c = 0.5$ K measured in GILD Si bulk samples of similar thickness $d = 30$ nm and active doping $n_B = 3 \times 10^{21}$ cm^{-3}[22] Expressing b in the free electron model $b = v_{F,S}/v_{F,N} = (n_N/n_S)^{1/3}$, we recover a concentration in the unmelted normal layer underneath the melted layer of $n_N = 3.75 \times 10^{20}$ cm^{-3}. This value is remarkably close to the equilibrium solubility limit $n_{sol} = 4 \times 10^{20}$ cm^{-3}, suggesting that a large fraction of the dopants present in the implantation queue ($>5.7 \times 10^{20}$ cm^{-3}) would be activated, up to the equilibrium saturation concentration, by the heat provided by the melted layer just above (the Si melting temperature being 1683 K).

While this two-parameters fit provides a coherent scenario, it is interesting to look at the results of the three parameters fit ($T_{c,0}$, b and d_S), relaxing the constraint about the superconducting thickness corresponding to the melted thickness, maintaining $d_N = d_{SOI} - d_S$. The fit is performed on the 1 shot samples, for which

a larger range and number of points are available (Fig. 4). A better agreement with the experimental data is then achieved, with $T_{c,0} = 1.04$ K, $b = 0.108$, and $d_S = d_{melt} - 16.6$ nm (Fig. 4). These fitting parameters suggest a scenario where the superconducting layer is only the top part of the melted layer, above the highest dislocation line, where the strain has been relaxed (Fig. S4). In this case, the normal layer is $d_N = d_{SOI} - d_{melt} + 16.6$ nm, which in the case of the samples shown in TEM analysis (Fig. 2) gives $d_N = 20.6$ nm, in agreement with the position of the dislocation line 17–21 nm above the BOX. Moreover, $T_{c,0}$ is in reasonable agreement with the maximum $T_c = 0.9$ K observed for $d_{melt} = 300$ nm thick bulk Si samples, where the influence of the thin, fully strained layer, can be neglected. In order to check if the identification of the superconducting layer with the relaxed one is also coherent in the case of the 5 shots samples, we have shown in Fig. 4 the $T_c(d_{melt})$ one parameter fit imposing the same $T_{c,0} = 1.04$ K and $d_N = d_{SOI} - d_{melt} + 9$ nm, again associating the superconducting layer to the relaxed region (for the sample shown in Fig. 2, this gives $d_N = 13$ nm in correspondence with the dislocation line 13 nm above the BOX). The resulting fitted $b = 0.29$ is then higher than the one estimated from 1 shot samples fit $b = 0.108$, in agreement with the larger B concentration expected in the bottom of the sample after five laser shots following the more homogeneous distribution of B for multiple laser shots. The fitting results are also coherent with the observation of a similar T_c between 1 and 5 laser shots, despite the larger average defect density for a single laser shot, as superconductivity would be established only in the topmost sublayer, where the crystalline quality is similar between 1 or a few anneals. These results highlight the importance of the structural strain relaxation in the establishment of Si superconductivity, in agreement with the recent results on bulk Si .[22,32]

CONCLUSIONS

In conclusion, we demonstrate superconducting monocrystalline Si epilayers with critical temperatures up to 0.5 K, obtained on 33 nm thick SOI 300 mm wafers after heavy pre-implantation of boron $(2.5 \times 10^{16}$ cm$^{-2})$, followed by nanosecond laser annealing with 25 ns pulse duration. Analysis of the transport properties (R, RRR, dose $\mathcal{N}$, T_c), coupled with structural measurements (XRD, $STEM$), have highlighted the effect of the nanosecond laser annealing energy and the impact of multiple laser anneals, both in the normal and superconducting phases. Increasing the laser energy allows increasing linearly T_c, through the increase in the melted thickness (and thus of the superconducting thickness), at a constant saturation active concentration of 6 at. % (corresponding to the out-of-equilibrium solubility limit attained by nanosecond laser annealing), while also improving the overall quality of the layer, its crystallinity and conductivity. The maximum T_c obtained, 0.5 K, is comparable with T_c of monocrystalline films of similar thickness obtained on bulk Si by gas immersion laser doping, where the dopants are introduced by "softer" chemisorption. This implies that nanosecond laser annealing can successfully heal the implantation-induced defects to recover good crystallinity from the initial amorphized phase. This supports the possibility of transferring the fabrication of nanosecond laser annealed superconducting layers from a laboratory environment toward more standard implantation-based doping techniques. Performing just a few laser anneals (5) instead of a single one reduces the amount of structural defects, such as stacking faults and dislocations, and homogenizes the B depth distribution. Finally, quantitative analysis of the results in the frame of superconductor/normal metal bilayer structures suggests the importance of the structural strain relaxation to achieve the superconducting phase, and demonstrates an excellent transparency between the layers, allowing the further development of superconducting devices on SOI with compatible large-scale integration tools.

SUPPLEMENTARY MATERIAL

The supplementary material contains the commented data on x-ray diffraction, showing the raw data and the evolution with E_L of the diffraction peak position, amplitude, and width, for both 1 and 5 laser anneals; the estimation of the layer thickness as a function of E_L obtained from three independent measurements of the time-resolved reflectivity, the square conductance, and the active surface dose; and the in-plane and out-of-plane lattice deformation profile extracted from the TEM measurements.

ACKNOWLEDGMENTS

AUTHOR DECLARATIONS

Conflict of Interest

The authors have no conflicts to disclose.

Author Contributions

Y. Baron: Investigation (supporting); Visualization (supporting). **J. L. Lábár**: Funding acquisition (equal); Investigation (equal); Visualization (supporting). **S. Lequien**: Investigation (supporting). **B. Pécz**: Funding acquisition (supporting). **R. Daubriac**: Resources (supporting). **S. Kerdilès**: Resources (lead). **P. Acosta Alba**: Resources (equal). **C. Marcenat**: Resources (equal). **D. Débarre**: Conceptualization (equal); Funding acquisition (equal); Investigation (equal); Methodology (equal); Supervision (equal). **F. Lefloch**: Conceptualization (equal); Formal analysis (equal); Funding acquisition (equal); Investigation (equal); Methodology (equal); Writing – original draft (equal). **F. Chiodi**: Conceptualization (equal); Formal analysis (equal); Funding acquisition (equal); Investigation (equal); Methodology (equal); Supervision (equal); Validation (equal); Visualization (equal); Writing – original draft (lead); Writing – review & editing (lead).

DATA AVAILABILITY

The data that support the findings of this study are available from the corresponding author upon reasonable request.

REFERENCES

[1] K. E. J. Goh, L. A. Krivitsky, and D. L. Polla, "Quantum technologies for engineering: The materials challenge," Mater. Quantum Technol. **2**(1), 013002 (2022).

[2] M. Polini, F. Giazotto, K. Chung Fong, I. M. Pop, C. Schuck, T. Boccali, G. Signorelli, M. D'Elia, R. H. Hadfield, V. Giovannetti, D. Rossini, A. Tredicucci, D. K. Efetov, F. H. L. Koppens, P. Jarillo-Herrero, A. Grassellino, and D. Pisignano, "Materials and devices for fundamental quantum science and quantum technologies," arXiv:2201.09260 (2022).

[3] "Qubits meet materials science," Nat. Rev. Mater. **6**(10), 869 (2021).

[4] N. P. de Leon, K. M. Itoh, D. Kim, K. K. Mehta, T. E. Northup, H. Paik, B. S. Palmer, N. Samarth, S. Sangtawesin, and D. W. Steuerman, "Materials challenges and opportunities for quantum computing hardware," Science **372**(6539), eabb2823 (2021).

[5] I. Siddiqi, "Engineering high-coherence superconducting qubits," Nat. Rev. Mater. **6**(10), 875–891 (2021).

[6] A. P. M. Place, L. V. H. Rodgers, P. Mundada, B. M. Smitham, M. Fitzpatrick, Z. Leng, A. Premkumar, J. Bryon, A. Vrajitoarea, S. Sussman, G. Cheng, T. Madhavan, H. K. Babla, X. H. Le, Y. Gang, B. Jäck, A. Gyenis, N. Yao, R. J. Cava, N. P. de Leon, and A. A. Houck, "New material platform for superconducting transmon qubits with coherence times exceeding 0.3 milliseconds," Nat. Commun. **12**(1), 1779 (2021).

[7] M. Vinet, "The path to scalable quantum computing with silicon spin qubits," Nat. Nanotechnol. **16**(12), 1296–1298 (2021).

[8] G. Scappucci, C. Kloeffel, F. A. Zwanenburg, D. Loss, M. Myronov, J.-J. Zhang, S. De Franceschi, G. Katsaros, and M. Veldhorst, "The germanium quantum information route," Nat. Rev. Mater. **6**(10), 926–943 (2020).

[9] S. G. J. Philips, M. T. Madzik, S. V. Amitonov, S. L. de Snoo, M. Russ, N. Kalhor, C. Volk, W. I. L. Lawrie, D. Brousse, L. Tryputen, B. P. Wuetz, A. Sammak, M. Veldhorst, G. Scappucci, and L. M. K. Vandersypen, "Universal control of a six-qubit quantum processor in silicon," Nature **609**, 919 (2022).

[10] F. Arute, K. Arya, R. Babbush, D. Bacon, J. C. Bardin, R. Barends, R. Biswas, S. Boixo, F. G. S. L. Brandao, D. A. Buell, B. Burkett, Y. Chen, Z. Chen, B. Chiaro, R. Collins, W. Courtney, A. Dunsworth, E. Farhi, B. Foxen, A. Fowler, C. Gidney, M. Giustina, R. Graff, K. Guerin, S. Habegger, M. P. Harrigan, M. J. Hartmann, A. Ho, M. Hoffmann, T. Huang, T. S. Humble, S. V. Isakov, E. Jeffrey, Z. Jiang, D. Kafri, K. Kechedzhi, J. Kelly, P. V. Klimov, S. Knysh, A. Korotkov, F. Kostritsa, D. Landhuis, M. Lindmark, E. Lucero, D. Lyakh, S. Mandrà, J. R. McClean, M. McEwen, A. Megrant, X. Mi, K. Michielsen, M. Mohseni, J. Mutus, O. Naaman, M. Neeley, C. Neill, M. Y. Niu, E. Ostby, A. Petukhov, J. C. Platt, C. Quintana, E. G. Rieffel, P. Roushan, N. C. Rubin, D. Sank, K. J. Satzinger, V. Smelyanskiy, K. J. Sung, M. D. Trevithick, A. Vainsencher, B. Villalonga, T. White, Z. J. Yao, P. Yeh, A. Zalcman, H. Neven, and J. M. Martinis, "Quantum supremacy using a programmable superconducting processor," Nature **574**(7779), 505–510 (2019).

[11] Y. Wu, W.-S. Bao, S. Cao, F. Chen, M.-C. Chen, X. Chen, T.-H. Chung, H. Deng, Y. Du, D. Fan, M. Gong, C. Guo, C. Guo, S. Guo, L. Han, L. Hong, H.-L. Huang, Y.-H. Huo, L. Li, N. Li, S. Li, Y. Li, F. Liang, C. Lin, J. Lin, H. Qian, D. Qiao, H. Rong, H. Su, L. Sun, L. Wang, S. Wang, D. Wu, Y. Xu, K. Yan, W. Yang, Y. Yang, Y. Ye, J. Yin, C. Ying, J. Yu, C. Zha, C. Zhang, H. Zhang, K. Zhang, Y. Zhang, H. Zhao, Y. Zhao, L. Zhou, Q. Zhu, C.-Y. Lu, C.-Z. Peng, X. Zhu, and J.-W. Pan, "Strong quantum computational advantage using a superconducting quantum processor," Phys. Rev. Lett. **127**, 180501 (2021).

[12] E. Bustarret, C. Marcenat, P. Achatz, J. Kacmarcik, F. Levy, A. Huxley, L. Ortega, E. Bourgeois, X. Blase, D. Débarre, and J. Boulmer, "Superconductivity in doped cubic silicon," Nature **444**(7118), 465–468 (2006).

[13] C. Marcenat, J. Kacmarcik, R. Piquerel, P. Achatz, G. Prudon, C. Dubois, B. Gautier, J. C. Dupuy, E. Bustarret, L. Ortega, T. Klein, J. Boulmer, T. Kociniewski, and D. Débarre, "Low-temperature transition to a superconducting phase in boron-doped silicon films grown on (001)-oriented silicon wafers," Phys. Rev. B **81**, 020501 (2010).

[14] F. Chiodi, A. Grockowiak, J. E. Duvauchelle, F. Fossard, F. Lefloch, T. Klein, C. Marcenat, and D. Débarre, "Gas immersion laser doping for superconducting nanodevices," in E-MRS 2013 Symposium V: Laser Material Interactions for Micro-and Nano-Applications 27-31 May 2013, Strasbourg, France [Appl. Surf. Sci. 302, 209–212 (2014)].

[15] R. Daubriac, P. A. Alba, C. Marcenat, S. Lequien, T. D. Vethaak, F. Nemouchi, F. Lefloch, and S. Kerdiles, "Superconducting polycrystalline silicon layer obtained by boron implantation and nanosecond laser annealing," ECS J. Solid State Sci. Technol. **10**, 014004 (2021).

[16] P. Dumas, M. Opprecht, S. Kerdilès, J. Lábár, B. Pécz, F. Lefloch, and F. Nemouchi, "Superconductivity in laser-annealed silicon films: The role of boron implant," Appl. Phys. Lett. **123**(13), 132602 (2023).

[17] J. E. Duvauchelle, A. Francheteau, C. Marcenat, F. Chiodi, D. Débarre, K. Hasselbach, J. R. Kirtley, and F. Lefloch, "Silicon superconducting quantum interference device," Appl. Phys. Lett. **107**(7), 072601 (2015).

[18] F. Chiodi, J.-E. Duvauchelle, C. Marcenat, D. Débarre, and F. Lefloch, "Proximity-induced superconductivity in all-silicon superconductor/normal-metal junctions," Phys. Rev. B **96**, 024503 (2017).

[19] F. Chiodi, R. Daubriac, and S. Kerdilès, "Laser ultra-doped silicon: Superconductivity and applications," in Laser Annealing Processes in Semiconductor Technology, Woodhead Publishing Series in Electronic and Optical Materials, edited by F. Cristiano and A. La Magna (Woodhead Publishing, 2021), Chap. 9, pp. 357–400.

[20] P. Bonnet, F. Chiodi, D. Flanigan, R. Delagrange, N. Brochu, D. Débarre, and H. le Sueur, "Strongly nonlinear superconducting silicon resonators," Phys. Rev. Appl. **17**, 034057 (2022).

[21] M. Posselt and J. P. Biersack, "Computer simulation of ion implantation into crystalline targets," Nucl. Instrum. Methods Phys. Res., Sect. B **64**, 706–710 (1992).

[22] L. Desvignes, "Laser ultra-doped superconducting silicon: From the material to the devices," Ph.D. thesis, Université Paris Saclay, 2023.

[23] M. O. Thompson, G. J. Galvin, J. W. Mayer, P. S. Peercy, J. M. Poate, D. C. Jacobson, A. G. Cullis, and N. G. Chew, "Melting temperature and explosive crystallization of amorphous silicon during pulsed laser irradiation," Phys. Rev. Lett. **52**, 2360–2363 (1984).

[24] R. F. Wood and G. E. Jellison, "Chapter 4 melting model of pulsed laser processing," Semicond. Semimetals **23**, 165–250 (1984).

[25] G. Hallais, G. Patriarche, L. Desvignes, D. Débarre, and F. Chiodi, "Stem analysis of deformation and b distribution in nanosecond laser ultra-doped Si:B," Semicond. Sci. Technol. **38**(3), 034003 (2023).

[26] H. K. Sy, D. K. Desai, and C. K. Ong, "Electron screening and mobility in heavily doped silicon," Phys. Status Solidi B **130**(2), 787–792 (1985).

[27] A. Grockowiak, T. Klein, H. Cercellier, F. Lévy-Bertrand, X. Blase, J. Kačmarčik, T. Kociniewski, F. Chiodi, D. Débarre, G. Prudon, C. Dubois, and C. Marcenat, "Thickness dependence of the superconducting critical temperature in heavily doped Si:B epilayers," Phys. Rev. B **88**, 064508 (2013).

[28] Y. V. Fominov and M. V. Feigel'man, "Superconductive properties of thin dirty superconductor–normal-metal bilayers," Phys. Rev. B **63**, 094518 (2001).

[29] S. Guéron, H. Pothier, N. O. Birge, D. Esteve, and M. H. Devoret, "Superconducting proximity effect probed on a mesoscopic length scale," Phys. Rev. Lett. **77**, 3025–3028 (1996).

[30] J. M. Martinis, G. C. Hilton, K. D. Irwin, and D. A. Wollman, "Calculation of TC in a normal-superconductor bilayer using the microscopic-based Usadel theory," Nucl. Instrum. Methods Phys. Res., Sect. A **444**(1–2), 23–27 (2000).

[31] L. Boeri, J. Kortus, and O. K. Andersen, "Three-dimensional MgB_2-type superconductivity in hole-doped diamond," Phys. Rev. Lett. **93**, 237002 (2004).

[32] S. Nath, I. Turan, L. Desvignes, L. Largeau, O. Mauguin, M. Túnica, M. Amato, C. Renard, G. Hallais, D. Débarre, and F. Chiodi, "Tuning superconductivity in nanosecond laser annealed boron doped $Si_{1-x}Ge_x$ epilayers," Phys. Stat. Solidi A 2400313 (published online) (2024).